Peer-reviewed version available at *Infrastructures* **2018**, *3*, 29; doi:10.3390/infrastructures3030029

Article

Surface Rust Detection Using Ultrasonic Waves in a Cylindrical Geometry by Finite Element Simulation

Qixiang Tang [1], Cong Du [2], Jie Hu[1], Xingwei Wang[2] and Tzuyang Yu [1,*]

[1] Department of Civil and Environmental Engineering, One University Avenue, Lowell, MA 01854, U.S.A.
[2] Department of Electric and Computer Engineering, One University Avenue, Lowell, MA 01854, U.S.A.
* Correspondence: tzuyang_yu@uml.edu; Tel.: +1-978-934-2288

Version July 10, 2018 submitted to Preprints

Abstract: Detection of early stage corrosion on slender steel members is crucial for preventing buckling failures of steel structures. An active photoacoustic fiber optic sensors (FOS) system has been reported for early stage steel corrosion detection of steel plates and rebars using surface ultrasonic waves. The objective of this paper is to investigate the surface corrosion/rust detection problem on steel rods using numerically simulated surface ultrasonic waves. The finite element method (FEM) is applied in simulating the propagation of ultrasonic waves on steel rod models. Transmission mode of damage detection is adopted, in which one source (transmitter) and one sensor (receiver) are considered. In this research, radial displacements at the receiver were simulated and analyzed by short-time Fourier transform (STFT) for detecting, locating, and quantifying a surface rust located between the transmitter and the receiver. From our time domain and frequency domain analyses, it is found that the presence, location, and dimensions (length, width, and depth) of surface rust can be estimated by ultrasonic waves propagating through the surface rust.

Keywords: finite element method (FEM); damage detection; surface rust; ultrasonic testing; short-time Fourier transform

1. Introduction

Slender steel members such as steel rods and bars are widely used structural components in civil infrastructure (e.g., steel truss bridges, temporary support structures, traffic signs). Unlike other construction materials such as Portland cement concrete, steel is vulnerable to corrosion. Steel corrosion can take place when suitable environmental conditions (e.g., temperature, pH, oxygen, moisture, chloride ions) are met. As a result, premature failures of steel structures can occur if one or many critical members is corroded. Corrosion of steel members will reduce the effective cross sectional area of the member by replacing steel (ferrite) with rust (ferrite oxides). Consequently, structural stiffness and bearing capacity of corroded steel members will be reduced. Furthermore, corrosion of steel members can also increase the likelihood of instability (buckling) for slender steel members, due to the change of boundary condition at the support or within each member.

Detection of early stage corrosion on slender steel members is crucial for preventing their premature failures. Various nondestructive evaluation/testing (NDE/T) and structural health monitoring (SHM) techniques have been applied to steel structures [1]. Example techniques include visual testing [2], modal analysis [3], Eddy current testing [4], thermal infrared testing [5], and ultrasonic testing [6,7]. Among these techniques, fiber optic sensors (FOS) represent a popular approach for long-term monitoring of steel structures [8,9]. While FOS have been applied to many steel structures in the past, most of the damage detection algorithms are based on passive response of FOS. In other words, either corrosion-induced cracking or loading-induced dynamic response must be generated from monitored steel members such that FOS can passively detect the presence of corrosion. Recently, an active photoacoustic FOS system has been reported for early stage steel corrosion detection of steel plates and rebars [10]. Different from traditional passive FOS techniques, active FOS can generate acoustic/ultrasonic waves to probe monitored steel members for early-stage corrosion detection.

Preprints (www.preprints.org) | NOT PEER-REVIEWED | Posted: 10 July 2018 doi:10.20944/preprints201807.0170.v1

Peer-reviewed version available at Infrastructures 2018, 3, 29; doi:10.3390/infrastructures3030029

Meanwhile, installed FOS allow engineers to assess the conditions (e.g., temperature) of structures without the use of couplant and "adapters" [11–13]. With a minimized size, active FOS can be installed onto irregular/curved surface of structures.

In this paper, our objective is to investigate the surface rust detection problem in a cylindrical geometry (slender steel rod) using ultrasonic waves in transmission mode and to develop a surface rust detection algorithm., as a basis for the practical application of an active photoacoustic FOS system. Steel rods are chosen as an example of slender steel members. The finite element method (FEM) is applied in simulating the propagation of ultrasonic waves at 1MHz on steel rod models. Surface rust is simulated by a rectangular prism which is characterized by its location (s_3), length (d), width (w), and depth (h). Transmission mode of damage detection is adopted, in which one source (transmitter) and one sensor (receiver) are considered. In this research, radial displacements ($u(t)$) at the receiver were simulated and analyzed by short-time Fourier transform (STFT) for detecting, locating, and quantifying a surface rust located between the transmitter and the receiver. Time domain and frequency domain analyses are conducted for developing a damage detection algorithm. In what follows, the detail of finite element (FE) simulation is first provided.

2. Finite element simulation

In the past, FEM had been applied for simulating ultrasonic wave propagation for damage detection [14–16]. Among various signal processing techniques, short-time Fourier transform (STFT) has been demonstrated as an applicable approach for analyzing the transient response of ultrasonic wave propagation in the time-frequency domain [17]. In this research, cylindrical geometry was numerically modeled by six steel rod models (one intact and five corroded) in a commercially available finite element package (ABAQUS 2016) [18]. 705, 600 linear hexahedral elements (C3D8) were used in all six models. Five corroded steel rod models were created by introducing a rectangular prism/anomaly to the surface of intact steel rod model. Transmission mode of damage detection was applied for data collection by using one transmitter (source or T) and one receiver (R) in each model, as shown in Fig. 1. Time domain radial displacement ($u(t)$) at the receiver was collected for all six models. Design of intact and corroded FE models are described in the following sections.

2.1. Intact steel rod model

An intact steel rod model (denoted by IM) was created by using a cylinder with 12.7-mm diameter (D) and 50-mm length, as shown in Fig. 1. Materials properties of steel used in the intact steel rod model was provided in Table 1. A transmitter (T) was located at mid-span and a receiver (R) was located 10 mm away from T along the longitudinal axis (z-axis) of the model. The distance between T and R was denoted as s_1. The intact steel rod model was fixed at both ends. To suppress unnecessary reflections from both ends, ten absorbing layers [19] were used at each end of the model such that ultrasonic waves propagating into the absorbing layers can be damped out. As shown in Fig. 2), a sinusoidal pulse was introduced at T, and time domain radial displacement ($u(t)$) was collected at R.

Table 1. Material's properties

Material	Density (kg/m^3)	Young's Modulus (MPa)	Poisson's Ratio
Steel	7,850	210,000	0.3
Rust	2,610	500	0.3

2.2. Corroded steel rod models

Five corroded steel rod models (denoted by CM) were generated by replacing the material properties at a corroded region from steel to rust in order to simulate the introduction of surface rust to the intact steel rod model, as shown in Table 2. Four attributes were used to characterize the corroded

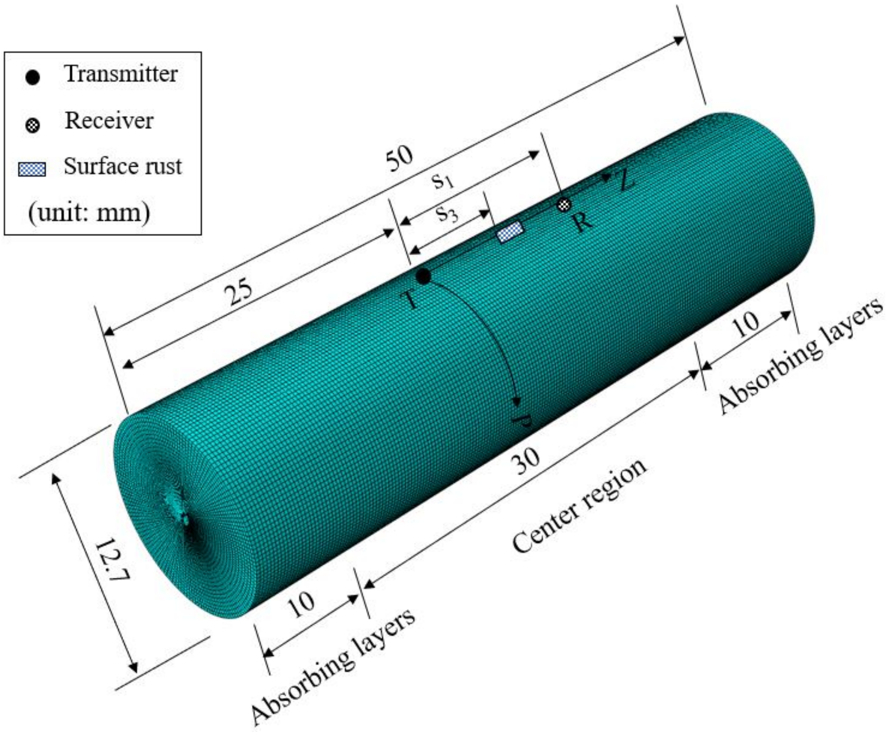

Figure 1. Intact steel rod model

region (surface rust): location (s_3), length (d), width (w) and thickness (h). Two values were considered for each attribute.

Table 2. Five corroded steel rod models

Model	Surface rust location s_3 (mm)	Surface rust length d (mm)	Surface rust width w (mm)	Surface rust thickness h (mm)
CM1	4	2	2.2	1
CM2	6	2	2.2	1
CM3	4	4	2.2	1
CM4	4	2	4.4	1
CM5	4	2	2.2	0.5

3. Research hypotheses and approach

3.1. Hypotheses of ultrasonic waves propagation in intact and corroded rod models

Five hypotheses on ultrasonic waves propagation in intact and corroded steel rod models were made for the damage detection problem in this paper. A Mercator projection of cylindrical geometry for steel rod models is provided in Fig. 3 to better illustrate these hypotheses.

1. In model IM, time domain radial displacement $u(t)$ is collected at R. The first ultrasonic wave packet is the one propagating along the $\vec{s}_1$ path at a velocity of c_1 and arriving at time t_1. The second ultrasonic wave packet propagates along the $\vec{s}_2$ path and arriving at time t_2 with a velocity of c_2.
2. In corroded steel rod models (CM1 CM5), the ultrasonic waves propagating along the $\vec{s}_1$ path are affected by the presence of surface rust. As shown in Fig. 3 (side view), part of the ultrasonic

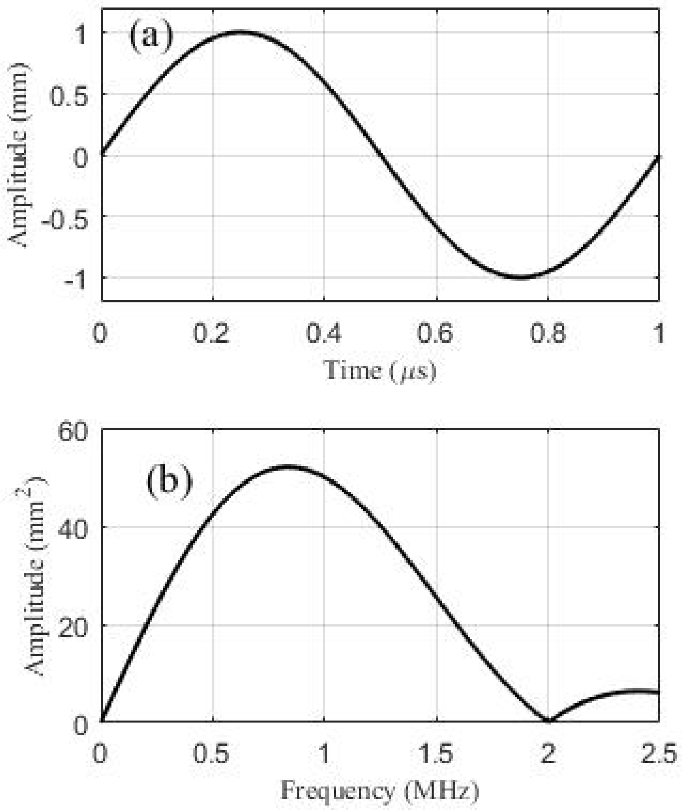

Figure 2. Designed loading function

waves propagates through the surface rust and arrives at time t_1' (i.e., $t_1'>t_1$ since the ultrasonic wave velocity in rust is slower than the one in steel).

3. Part of the ultrasonic waves is scattered from the surface rust and propagates along the $\vec{s}_4$ path. Time t_2' is the total time of flight (TOF) of scattered ultrasonic wave propagating along path $(\vec{s}_3, \vec{s}_4)$ ($t_2' = t_3 + t_4$). Propagation velocities of ultrasonic waves on path $\vec{s}_1$ and path $(\vec{s}_3, \vec{s}_4)$ are respectively c_1' and c_2'.
4. In Fig. 3 (top view), path $\vec{s}_8$ is the path of ultrasonic waves diffracted by the surface rust ($\vec{s}_8 = \vec{s}_6 + d + \vec{s}_7$). TOF of these ultrasonic waves is t_8 (i.e., $t_8 = t_6 + t_d + t_7$).
5. Higher frequencies are affected more than lower frequencies by the presence of surface rust. This is because that the effective depth of each frequency is approximately its wavelength [20]. With 'shallow' effective depth, higher frequencies interact with the surface rust more than lower frequencies.

3.2. Damage detection algorithm

Based on the aforementioned five hypotheses, surface rust detection, localization and quantification are carried by the following approach.

3.2.1. Damage detection

In this paper, detection of surface rust can be accomplished by determining the reduction of centroid frequency (Δf_c) in the spectrogram of $u(t)$ by using STFT. The steps of obtaining f_c are reported in the following.

1. Generate/introduce ultrasonic waves at transmitter T of model IM.

Preprints (www.preprints.org) | NOT PEER-REVIEWED | Posted: 10 July 2018 doi:10.20944/preprints201807.0170.v1

Peer-reviewed version available at Infrastructures 2018, 3, 29; doi:10.3390/infrastructures3030029

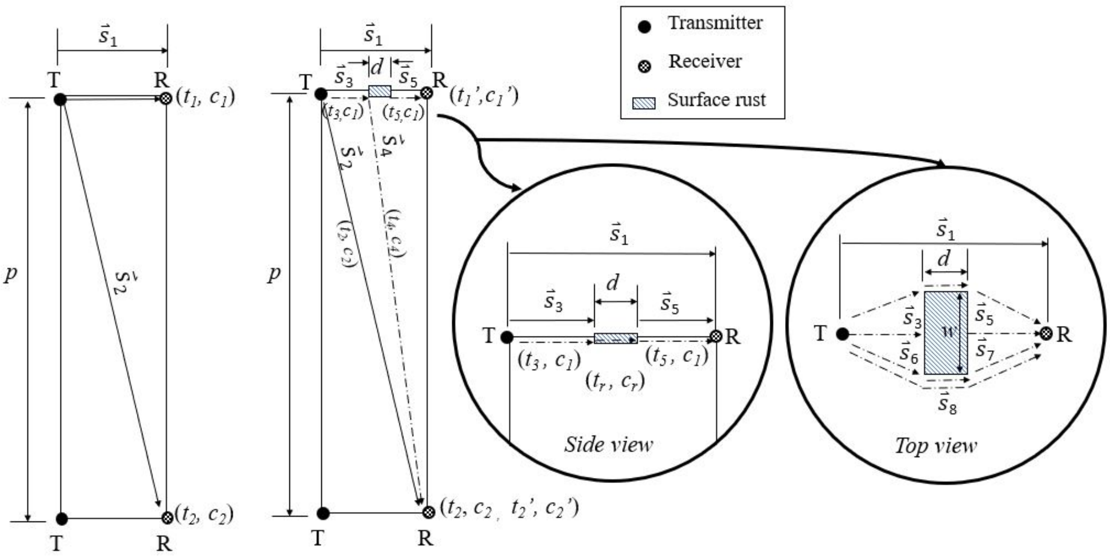

Figure 3. Mercator projection of intact and corroded surface for ultrasonic wave propagation paths

2. Collect time domain radial displacement $u(t)$ at receiver R.
3. Apply short-time Fourier transform (STFT) to $u(t)$ in order to convert it to its spectrogram $U(t, f)$.
4. In the spectrogram $U(t, f)$, show the half-power contour at -3 dB from the maximum amplitude of the first wave packet.
5. Determine the centroid of the half-power contour for the first wave packet by finding its coordinates (f_c, t_c) in the spectrogram $U(t, f)$.
6. The centroid frequency f_c of this FE simulation is found. For intact model (IM), $f_c = f_{c,i}$.
7. Repeat the steps for an artificially corroded model. For corroded models, $f_c = f_{c,c}$.

Fig. 4 illustrates the parameters defined in the steps for damage detection, using model CM1 as an example. Eq. (1) shows the damage detection criterion for detecting the presence of surface rust.

$$\Delta f_c = f_{c,i} - f_{c,c} \begin{cases} = 0 & \text{intact} \\ \neq 0 & \text{corroded} \end{cases} \tag{1}$$

where Δf_c = difference in the centroid frequency between intact and corroded steel rod models (in MHz), $f_{c,i}$ = centroid frequency of model IM (in MHz), and $f_{c,c}$ = centroid frequency of corroded steel rod models (in MHz). In this research, a steel rod model is considered intact (no damage) if there is no reduction of centroid frequency or $\Delta f_c = 0$ and vice versa.

3.2.2. Damage localization

To locate surface rust, TOF (time-of-flight) of scattered ultrasonic waves is used. In this research, the location of surface rust is defined by the length of path $\vec{s}_3$ or $s_3 = |\vec{s}_3|$. The value of s_3 indicates the location of surface rust.

TOF of the scattered wave (t'_2) traveling through path $\vec{s}_3$ and $\vec{s}_4$ is defined by

$$t'_2 = t_3 + t_4 \tag{2}$$

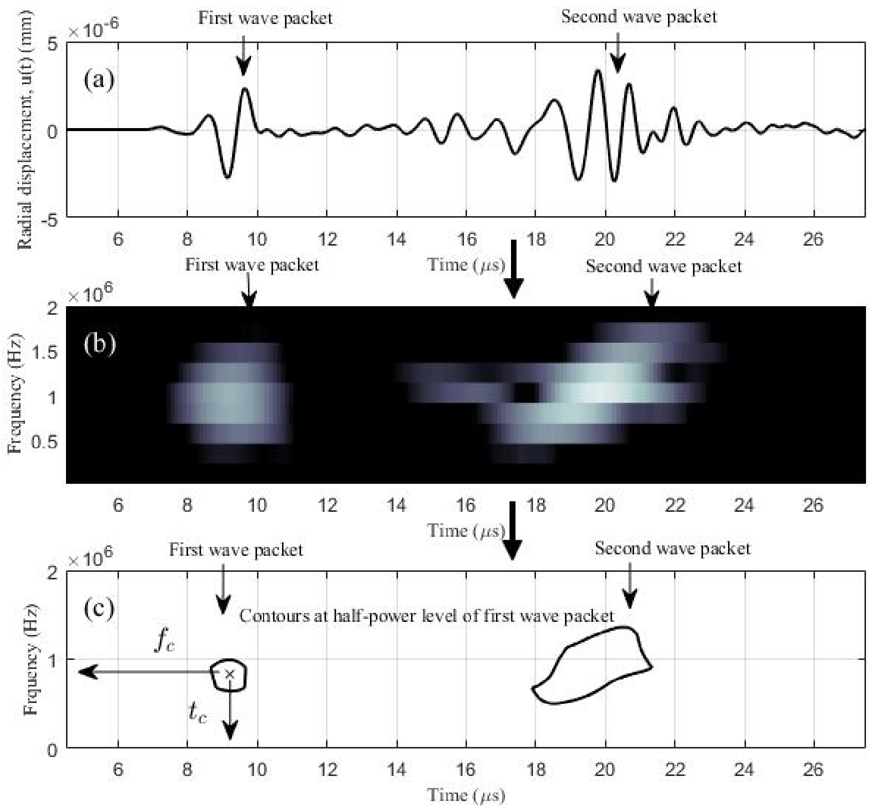

Figure 4. Procedure of obtaining f_c value

131 where t_3 and t_4 = TOF of ultrasonic waves propagating on paths $\vec{s}_3$ and $\vec{s}_4$ (μs)), respectively.
132 Equivalently,

$$t_2'(s_3, s_4) = \frac{s_3}{c_1} + \frac{s_4}{c_4} \tag{3}$$

133 where s_3 = length of path $\vec{s}_3$ (mm), $s_4(s_3)$ = length of path $\vec{s}_4$ (mm) = $\sqrt{(s_1 - s_3)^2 + p^2}$, p = perimeter
134 of the rod model (mm), c_1 = propagation velocity on path $\vec{s}_1$ (mm/μs), and c_4 = propagation velocity
135 on path $\vec{s}_4$ (mm/μs). From our previous study, a propagation velocity model (Eq. (4)) based on the
136 length of path on a cylindrical geometry was reportedc_4 [17].

$$c_4(s_4) = a + b\left(\frac{p}{s_4}\right) \tag{4}$$

137 where a and b = model parameters. By substituting Eq. (4) and re-arranging terms, we have

$$\left[(s_1 - s_3)^2 + p^2\right] c_1 - (t_2' - s_3 a)\sqrt{(s_1 - s_3)^2 + p^2} - t_2' c_1 bp + s_3 bp = 0 \tag{5}$$

138 where s_1 = length of path $\vec{s}_1$ (mm). In Eq. (5), s_1, p, and c_1 must be provided. Parameters a and b
139 are from reported literature [17]. Time t_2' is measured from a corroded model. Once time t_2' is measured,
140 Eq. (5) can be solved by the graphic method. Eq. (5) also represents the damage localization criterion
141 in our algorithm. Finding the value of s_3 locates the surface rust in this research.

Preprints (www.preprints.org) | NOT PEER-REVIEWED | Posted: 10 July 2018 doi:10.20944/preprints201807.0170.v1

Peer-reviewed version available at Infrastructures 2018, 3, 29; doi:10.3390/infrastructures3030029

3.2.3. Damage quantification

For damage quantification, dimensions of surface rust (length d, width w, and thickness h) are to be found. In finding the length d of surface rust, TOF (t'_1) of ultrasonic waves propagating through surface rust and arriving at receiver R is used. Time t'_1 denotes the total propagation time along path $\vec{s}_1$ which consists of path $\vec{s}_3$, surface rust (length d), and path $\vec{s}_5$. In other words,

$$t'_1 = t_3 + t_5 + t_r \tag{6}$$

where t'_1 = total TOF of ultrasonic wave propagating on path $\vec{s}_1$ (μs), t_3 = TOF of ultrasonic wave traveling on path $\vec{s}_3$ (μs), t_5 = TOF of ultrasonic wave traveling on path $\vec{s}_5$ (μs)), and t_r = TOF of ultrasonic wave traveling within surface rust (μs). Since $s_1 = s_3 + d + s_5$, we have

$$t'_1(d) = \frac{s_1 - d}{c_1} + \frac{d}{c_r} \tag{7}$$

where c_r = propagation velocity on z-axis in rust (mm/μs). By re-arranging Eq. (7), surface rust length d can be directly determined by

$$d(t'_1) = \frac{c_r s_1 - c_r c_1 t'_1}{c_r - c_1} \tag{8}$$

Eq. (7) represents the **length estimation** criterion in our algorithm.

Once s_3 (from damage localization, Eq. (5)) and d (from Eq. (8)) are determined, the width of surface rust (w) can be obtained by using the delayed arrival time of first wave packet (t_8), as shown in Fig. 3 (top view). Eq. (9) describes the relationship between t_8 and w.

$$t_8 c_1 - \sqrt{s_3^2 + (w/2)^2} - d - \sqrt{s_5^2 + (w/2)^2} = 0 \tag{9}$$

where $s_5 = s_1 - d - s_3$, t_8 = TOF of ultrasonic wave propagating on path $\vec{s}_8$ and

$$\vec{s}_8 = \vec{s}_6 + d + \vec{s}_7 \tag{10}$$

in a corroded steel rod model (μs), s_6 = length of path $\vec{s}_6$ (mm) and s_7 = length of path $\vec{s}_7$ (mm). Eq. (9) represents the **width estimation** criterion in our algorithm.

From our fifth hypothesis (Section 3.1), lower frequency ultrasonic waves have 'deeper' effective depths. It suggests that more frequencies in the STFT spectrogram will be affected when increasing the thickness h of surface rust. This phenomenon is illustrated by the reduction of spectrograms' curvature or $\frac{\partial^2 U_1}{\partial f^2}$ and modeled by an empirical equation as shown in Eq. (11).

$$h\left(\frac{\partial^2 U_1}{\partial f^2}\right) = e\frac{\partial^2 U_1}{\partial f^2} + g \tag{11}$$

where h = thickness of surface rust (mm), $\frac{\partial^2 U_1}{\partial f^2}$ = second-order partial derivative of the first wave packet's frequency domain projection, and e and g = model parameters. $\frac{\partial^2 U_1}{\partial f^2}$ approximates the curvature of the first wave packet. Eq. (11) represents the **thickness estimation** criterion in our algorithm.

Eqs. (8), (9) and (11) represent our damage quantification approach in this paper. Surface rust length d, width w, and thickness h can be estimated from the STFT spectrogram of radial displacement $u(t)$ measured at receiver R. In the following section, FE simulation results are reported.

Preprints (www.preprints.org) | NOT PEER-REVIEWED | Posted: 10 July 2018 doi:10.20944/preprints201807.0170.v1

Peer-reviewed version available at Infrastructures 2018, 3, 29; doi:10.3390/infrastructures3030029

4. Simulation results and findings

Time domain radial displacement ($u(t)$) of each model at receiver R was collected from six FE simulation cases (one for intact model and five for corroded models). Spectrogram ($U(f,t)$) of each $u(t)$ was obtained by STFT. Comparison of $u(t)$ and $U(f,t)$ between intact and corroded steel rod models was made to study the effects of surface rust on $u(t)$ and $U(f,t)$.

4.1. Time domain response

In each model, radial displacement $u(t)$ are receiver R was collected as shown in Fig. 5. As predicted by the first hypothesis, two wave packets were observed. The first wave packet was the ultrasonic wave propagating along the longitudinal direction (z-axis). The second wave packet was the ultrasonic wave propagating along the helical direction (i.e., $\vec{s}_2$ in Fig. 3). The waveform of the second wave packet is more complicated than the one of the first wave packet in the spectrogram, owing to the geometric dispersion (in the second wave packet) caused by the cylindrical geometry of FE models.

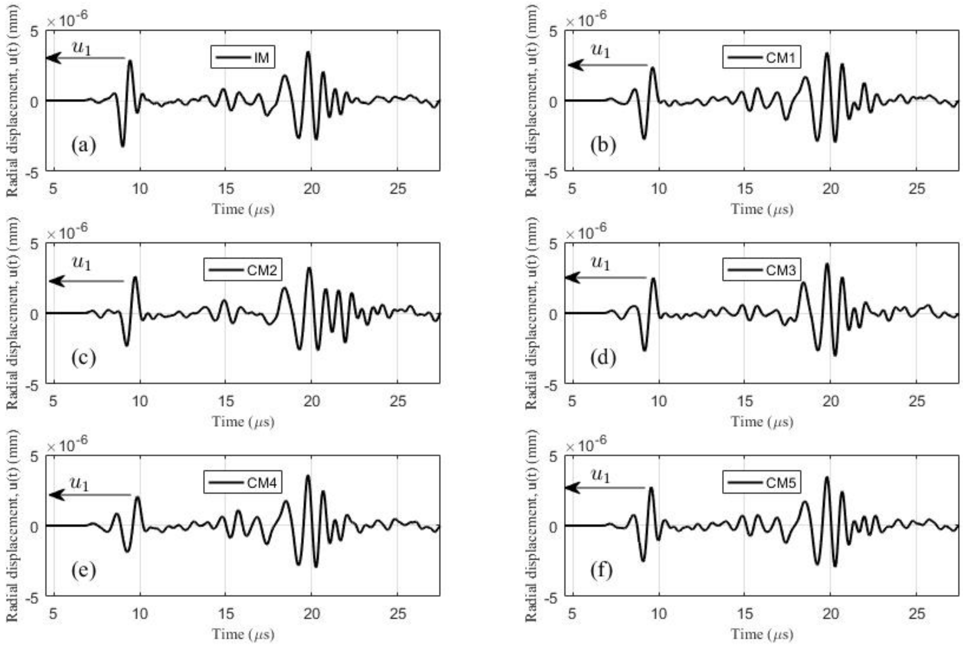

Figure 5. Time domain radial displacement in intact and corroded steel rod models

In corroded steel rod models (CM1 - CM5), the first peak amplitude (u_1) was reduced after interacting with surface rust and propagating on path $\vec{u}_1$. While the presence of surface rust can be detected by the reduction of u_1, quantification of surface rust using u_1 can be very difficult due to the geometric dispersion effect on $u(t)$. In reality, peak amplitudes can also be contaminated by background noise (e.g., ambient vibration). Therefore, frequency domain analysis of $u(t)$ is applied and described in the next section.

4.2. Time-frequency domain response

By applying STFT to $u(t)$, frequency change in $u(T)$ over time was shown on its spectrograms. Frequency range on the STFT spectrogram between 0.1 MHz and 2 MHz was determined, since this frequency range included most of the kinetic energy of transmitted ultrasonic waves.

Fig. 6 shows the STFT spectrogram of $u(t)$ at transmitter T of model IM. In Fig. 6, the first wave packet (white-colored vertical shape) represented the transmitted ultrasonic wave traveling in the longitudinal direction or path $\vec{s}_1$ (without geometric dispersion), whose amplitudes confirm our choice

Preprints (www.preprints.org) | NOT PEER-REVIEWED | Posted: 10 July 2018 doi:10.20944/preprints201807.0170.v1

Peer-reviewed version available at *Infrastructures* **2018**, *3*, 29; doi:10.3390/infrastructures3030029

on frequency range. The second wave packet (gray-colored tilted shape) represented the transmitted ultrasonic wave traveling in the helical direction (with geometric dispersion) and coming back to transmitter T. Due to the geometric dispersion in this FE simulation, ultrasonic waves at lower frequencies ($f < 1$ MHz) travel faster than the ones at higher frequencies ($f > 1$ MHz). This explains the tilted shape of the second wave packet.

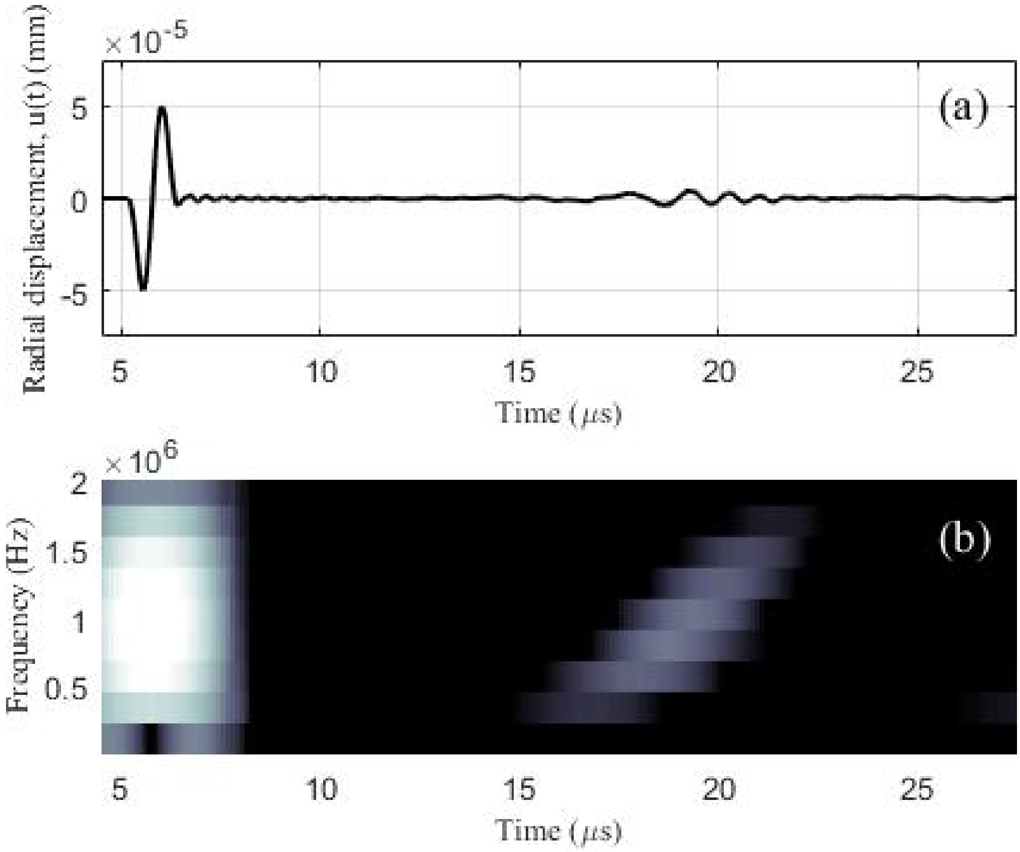

Figure 6. Radial displacement and spectrogram of the intact steel rod model at transmitter T

Fig. 7 shows the STFT spectrograms of $u(t)$ at receiver R of all six models. In Fig. 7, two wave packets were observed within the time window of 4.5 - 27.5 μs. The first wave packet centering at 8 μs represented the ultrasonic wave (vertical shape) propagating from transmitter T to receiver R along the longitudinal direction (z-axis). The second wave packet (tilted shape) represented the ultrasonic wave propagating along the helical direction or path $\vec{s}_2$. Fig. 8 shows the contours at the half-power level of the first wave packet in each spectrogram. In corroded steel rod models (CM1 CM5), higher frequencies in the first wave packet were reduced due to smaller effective depth. In addition, shape of the second wave packet changed due to the size change of surface rust, as shown in Fig. 8.

4.3. Surface rust detection

Detection of surface rust in a corroded steel rod model was accomplished by comparing its centroid frequency f_c with the one of an intact model (IM). Fig. 9 compares the half-power contours of intact (model IM) and corroded (models CM1 CM5) FE models in individual STFT spectrogram at receiver R. Center of the half-power contour of model IM was denoted by centroid frequency $f_{c,i}$. For five other corroded models, their centroid frequency was denoted by $f_{c,c}$ with different values. After finding $f_{c,i}$ and $f_{c,c}$, their difference Δf_c was calculated and reported in Table 3. Based on Eq. (1), the presence of surface rust in these models were detected.

Preprints (www.preprints.org) | NOT PEER-REVIEWED | Posted: 10 July 2018 doi:10.20944/preprints201807.0170.v1

Peer-reviewed version available at *Infrastructures* **2018**, *3*, 29; doi:10.3390/infrastructures3030029

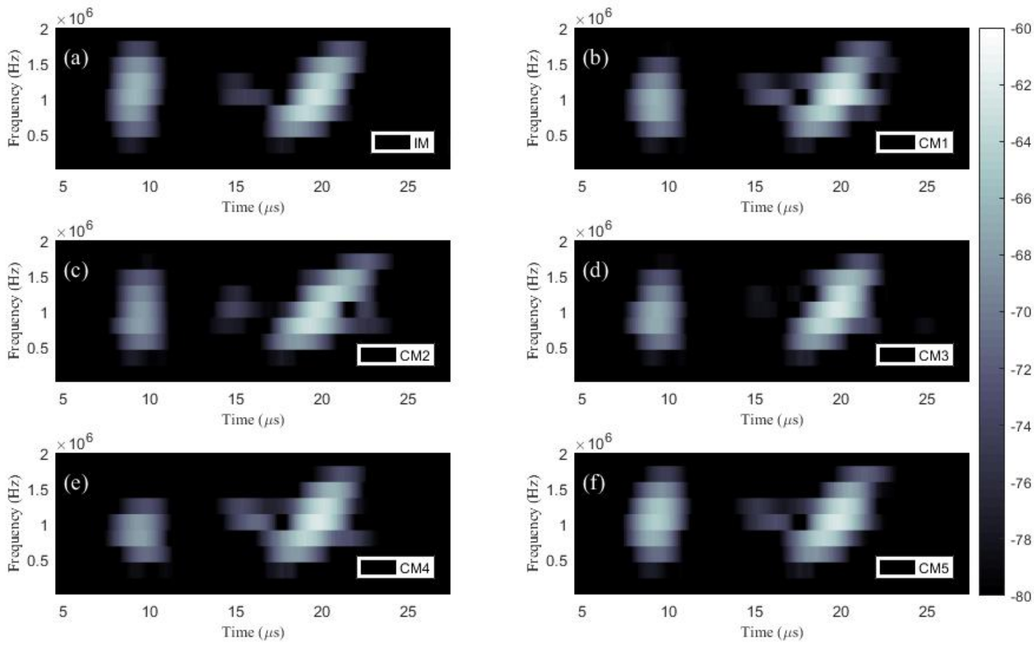

Figure 7. Spectrogram of intact and corroded steel rod models at receiver R

Table 3. Centroid frequency (f_c) of half-power contour for all models

Model	f_c **(MHz)**	Δf_c **(MHz)**
IM	1.00	0
CM1	0.83	0.17
CM2	0.83	0.17
CM3	0.82	0.18
CM4	0.82	0.18
CM5	0.80	0.20

4.4. Surface rust localization

Eq. (3) was used to locate surface rust in our simulations. In view of the presence of geometric dispersion in $u(t)$, measuring TOF in the time domain became challenging. To avoid the problem of chasing multiple frequencies at a time, the center frequency of transmitted ultrasonic wave in the STFT spectrogram (i.e., 1 MHz in this paper) was chosen.

Fig. 10 shows the STFT spectrogram (at 1MHz) of model IM at receiver R to demonstrate how to calculate the TOF of the scattered wave (t_2') traveling through paths $\vec{s}_3$ and $\vec{s}_4$. In Fig. 10 (a), the 1-MHz curves on the STFT spectrogram of model IM and model CM1 were extracted. Time t_1 denoted the TOF of the first wave packet and time t_2 the second wave packet for model IM. In Fig. 10, t_1 and t_2 were measured from the time t_0 when the ultrasonic wave was introduced at transmitter T; in this paper, $t_0 = 6.13\mu$s. Since the peak amplitude of the first wave packet was 9.01 μs, $t_1 = (9.01 - 6.13)\mu$s = 2.88μs. With traveling distance s_1 being 10 mm, the wave velocity c_1 can be calculated by

$$c_1 = \frac{s_1}{t_1} \tag{12}$$

$$\Rightarrow c_1 = \frac{10}{2.88} = 3.47 \quad \text{mm}/\mu s, \tag{13}$$

Preprints (www.preprints.org) | NOT PEER-REVIEWED | Posted: 10 July 2018 doi:10.20944/preprints201807.0170.v1

Peer-reviewed version available at *Infrastructures* **2018**, *3*, 29; doi:10.3390/infrastructures3030029

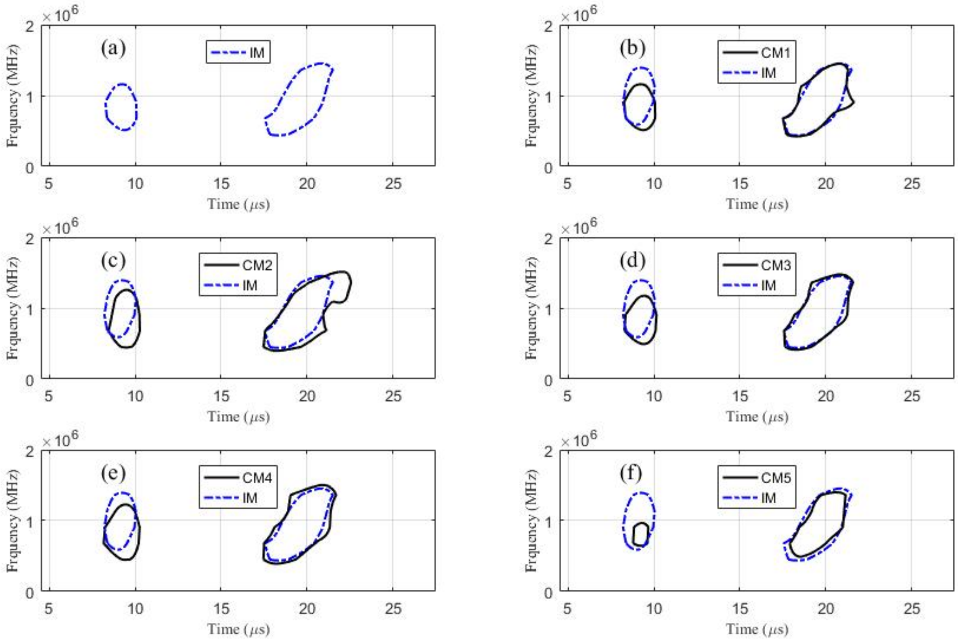

Figure 8. Half-power contours in STFT spectrogram for six models at receiver *R*

This wave velocity can be compared with the theoretical surface wave velocity c_t. c_t can be approximated by [21]

$$c_t \approx \frac{0.87 + 1.2\nu}{1+\nu}\sqrt{\frac{E}{2\rho(1+\nu)}} \tag{14}$$

With E = 210,000 MPa, ρ = 7,850 kg/m^3, and ν = 0.3, approximated theoretical c_t value was found to be 3.03mm/μs. Consequently, theoretical TOF t_t for the first wave packet was found to be

$$t_t = \frac{s_1 - z_l}{c_t} \tag{15}$$

$$\Rightarrow t_t = 3.14\mu s \tag{16}$$

where s_1 = distance from center of transmitter T to receiver R (mm) (= 10 mm) and z_l = distance from center of transmitter T to the edge of loading area at T (mm) (= 0.5 mm). An error of 8.2% was obtained between the approximated theoretical c_t value and numerical c_1 value.

A subtracted/differential 1-MHz curve (subtract model IM from model CM1) was generated and shown in Fig. 10 (b) from where differential TOF values of the first wave packet t'_1 and of the second packet t'_2 were determined to be $15.16 - t_0 = 9.03$ μs and $22.28 - t_0 = 22.28 - 6.13 = 16.15$ μs, respectively. In our algorithm, differential TOF of the second wave packet t'_2 was used for surface rust localization.

From the differential 1-MHz curve in Fig. 10 (b), a propagation velocity model from literature [17] for elastic waves on a cylindrical geometry was used.

$$c_4(s_4) = 3.47 - 0.8348\left(\frac{p}{s_4}\right) \tag{17}$$

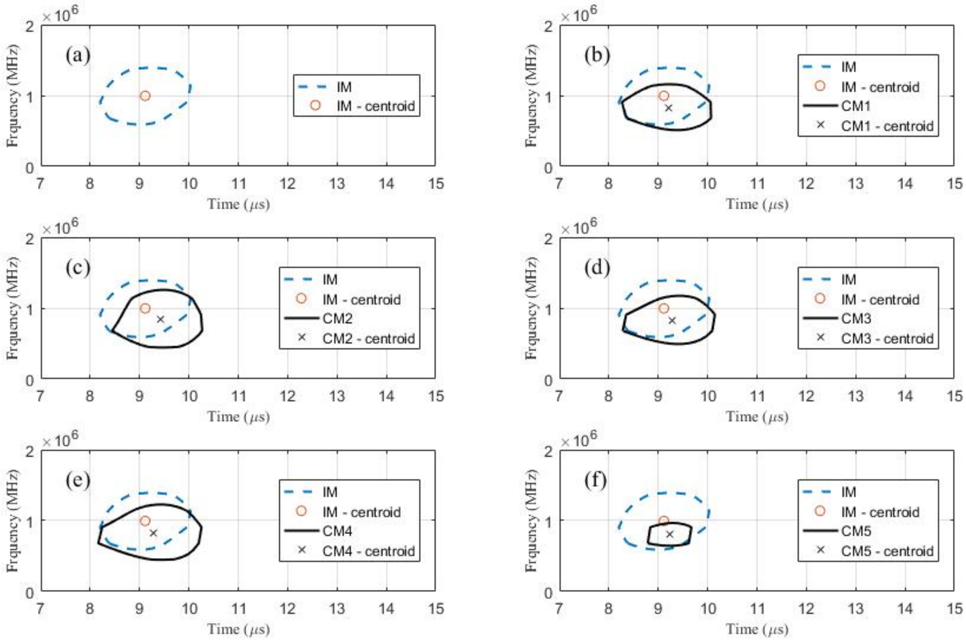

Figure 9. Half-power contours of the first wave packet at receiver R

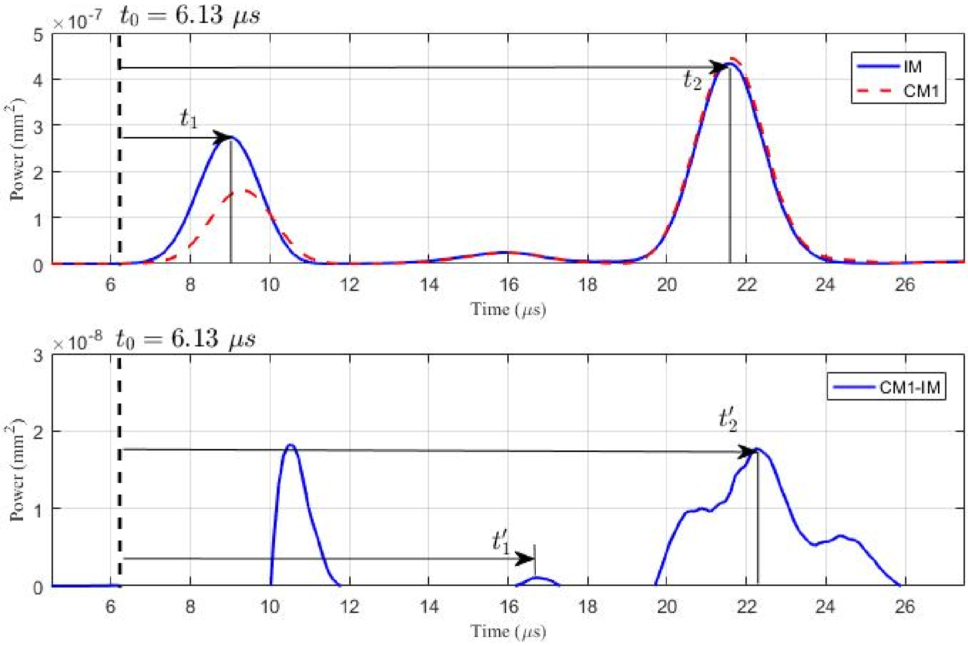

Figure 10. Spectrograms of model IM and model CM1 at 1 MHz

In all six FE models, $p = 12.7\pi = 39.9$ mm. From the Mercator projection shown in Fig. 3, it is clear that

$$s_4 = \sqrt{(d + s_5)^2 + p^2} \tag{18}$$

$$\Rightarrow s_4 = \sqrt{(s_1 - s_3)^2 + p^2} \tag{19}$$

Peer-reviewed version available at Infrastructures 2018, 3, 29; doi:10.3390/infrastructures3030029

With s_1 = 10 mm, p = 39.9 mm, c_1 = 3.47 mm/μs, a = 3.47, $b = -0.8348$, Eq. (5) could be written as

$$3.47\left[(10-s_3)^2+39.9^2\right]-(t_2'-3.47s_3)\sqrt{(10-s_3)^2+39.9^2}+155.58t_2'-33.31s_3=0 \tag{20}$$

$$\Rightarrow 5871.27-\left(102.71-\sqrt{20371.8-240.8s_3+12.04s_3^2}\right)s_3+3.47s_3^2$$
$$+\left(155.58-\sqrt{1692.01-20s_3+s_3^2}\right)t_2'=0 \tag{21}$$

Eq. (21) provides the condition between s_3 and t_2'. With differential TOF t_2', surface rust location s_3 can be found from Eq. (21). Since Eq. (21) cannot be solved analytically, the graphic method was applied with its result shown in Fig. 11. Eq. (21) represents a model for locating the surface rust in our algorithm. Following the same procedure, 1-MHz curves of models CM2 and CM3 were generated

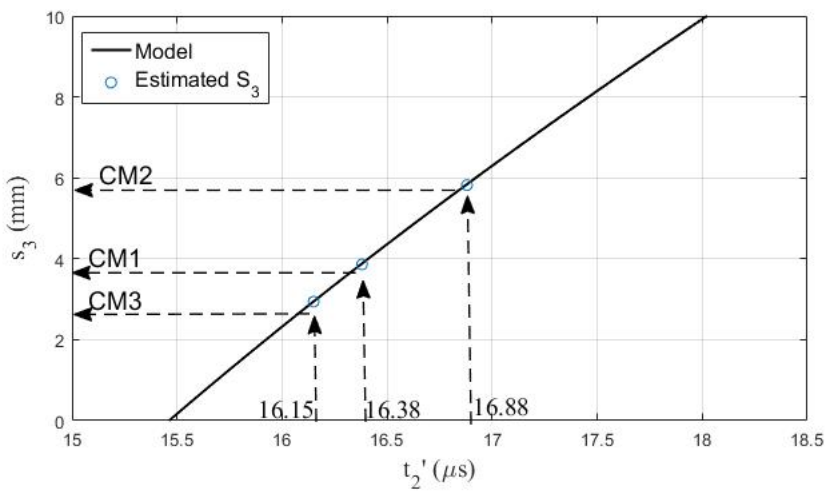

Figure 11. Relationship between s_3 and t_2'

(similar to Fig. 10 (b) for model CM1) in order to determine different TOF for models CM2 and CM3. For model CM2, t_2' was found by $22.51 - t_0 = 22.51 - 6.13 = 16.38\mu$s. For model CM3, t_2' was found by $23.01 - t_0 = 23.01 - 6.13 = 16.88\mu$s. Once t_2' was found, Eq. (21) can be used for finding surface rust location s_3.

Estimated surface rust locations (s_3) in corroded steel rod models was reported in Table 4.

Table 4. Comparison between predicted and actual location and dimensions

	Model	Predicted (mm)	Actual (mm)	Error(%)
Location, s_3	CM1	3.86	4	3.5
	CM2	5.91	6	1.5
	CM3	2.92	3	2.6
Length, d	CM1	1.97	2	1.5
	CM2	3.69	4	7.75
Width, w	CM1	2.36	2.2	7.27
	CM4	4.2	4.4	4.54
Thickness, h	CM1	0.98	1	2
	CM5	0.53	0.5	6

Preprints (www.preprints.org) | NOT PEER-REVIEWED | Posted: 10 July 2018 doi:10.20944/preprints201807.0170.v1

Peer-reviewed version available at Infrastructures 2018, 3, 29; doi:10.3390/infrastructures3030029

4.5. Surface rust quantification

For surface rust quantification, Eq. (8) was used to determine surface rust length d for models CM1 and CM2 by using measured time t_1'. Eq. (9) was applied to determine surface rust width w for models CM1 and CM4 by using measured time t_8'. Eq. (11) was utilized to determine surface rust depth h for models CM1 and CM5 by using measured curvature $\left(\dfrac{d^2U_1}{df^2}\right)$.

For determining surface rust length d by using Eq. (8), s_1 = 10 mm and propagation velocity in steel c_1 = 3.47 mm/μs (from Eq.(13)). Propagation velocity in rust c_r was calculated by $0.08454c_t = 0.257$ mm/μs from [20]. Therefore, Eq. (8) became

$$d(t_1') = \frac{0.257(10) - 0.257(3.47)t_1'}{3.47 - 0.257} \tag{22}$$

$$\Rightarrow d(t_1') = \frac{2.57 - 0.892t_1'}{3.213} \tag{23}$$

For model CM1, t_1' was found by $16.10 - t_0 = 16.10 - 6.13 = 9.97\mu$s. For model CM2, t_1' was found by $22.31 - t_0 = 22.31 - 6.13 = 16.18\mu$s. With Eq. (23), estimated surface rust length d for models CM1 and CM2 were reported 1.97 mm and 3.69 mm, respectively.

was applied to determine surface rust length d for models CM1 and CM2. With s_3 (from surface rust localization) and d found, surface rust width w values for models CM1 and CM4 were determined by solving Eq. (9) with measured t_8 (TOF of the first wave wave packet as shown in Fig. 12).

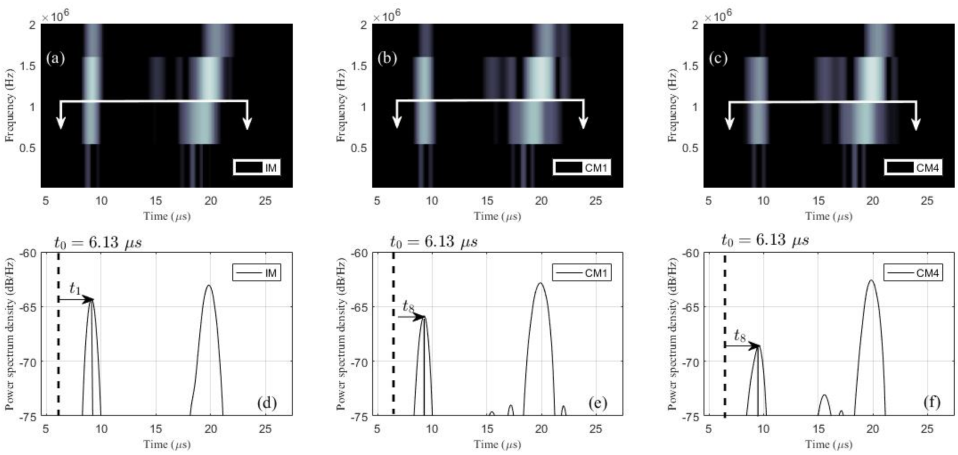

Figure 12. Time delay of the first wave packet

For surface rust width w quantification, estimated s_3 and d were substituted into Eq. (9). For example, in model CM1, Eq. (9) became

$$t_8 3.47 - \sqrt{3.86^2 + (w/2)^2} - 1.97 - \sqrt{(10 - 3.86 - 1.97)^2 + (w/2)^2} = 0 \tag{24}$$

where t_8 was found by $9.11 - t_0 = 9.11 - 6.13 = 2.98\mu$s. Surface rust width w values for model CM1 was hence determined to be 2.36 mm. Similarly,

$$t_8 3.47 - \sqrt{3.91^2 + (w/2)^2} - 1.98 - \sqrt{(10 - 3.91 - 1.97)^2 + (w/2)^2} = 0 \tag{25}$$

was obtained for models CM4. t_8 was found by $9.31 - t_0 = 9.31 - 6.13 = 3.18\mu s$ in CM4. Predicted w is 4.2 mm as shown in Table 4.

At last, curvature values of the first wave packet for models IM ($\frac{\partial^2 U_1}{\partial f^2} = -4.22 \times 10^5$), CM1 ($\frac{\partial^2 U_1}{\partial f^2} = -5.12 \times 10^5$), and CM5 ($\frac{\partial^2 U_1}{\partial f^2} = -4.72 \times 10^5$) were calculated from Fig. 13 (a). These curvature values were modeled with surface rust depth h by Eq. (11) to obtain model parameters $e = -1.1053 \times 10^5$ and $g = -4.6818$ ($R^2 = 0.996$). Therefore, Eq. (11) was written as

$$h\left(\frac{\partial^2 U_1}{\partial f^2}\right) = -1.1053 \times 10^5 \times \frac{\partial^2 U_1}{\partial f^2} - 4.6818 \tag{26}$$

Performance of proposed algorithm (Eqs. (23), (24), (25) and (26)) for surface rust quantification was summarized in Table 4.

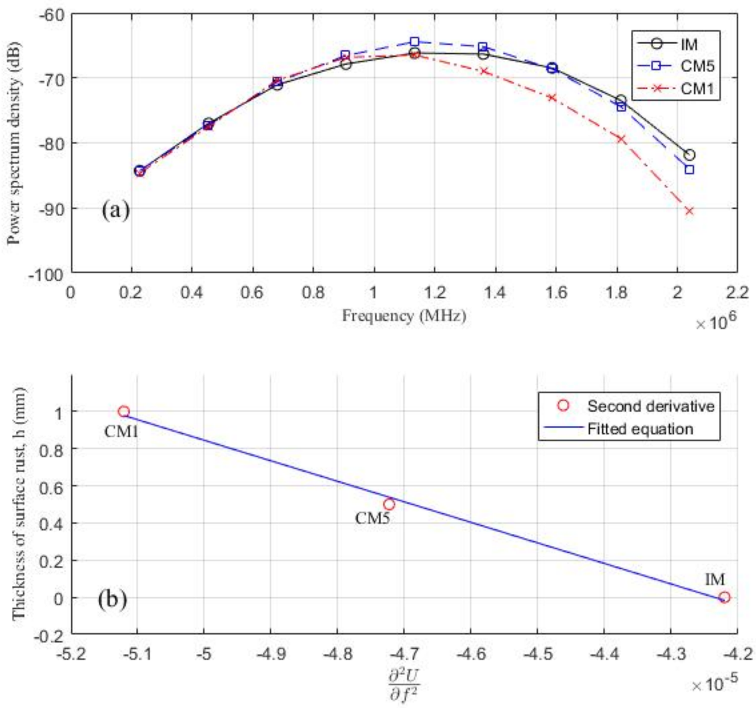

Figure 13. Ridge of the first wave packets and their second-order derivatives

4.6. Findings

By conducting the FE analysis of ultrasonic wave propagation in intact and corroded steel rod models, following research findings are obtained: (1) in the time domain, the first peak amplitude (u_1) is reduced due to the presence of a surface rust; (2) in the STFT spectrogram, shape of the second wave packet in the spectrogram is tilted due to the geometric dispersion in ultrasonic waves; (3) the first wave packet in corroded steel rod models suffered from high frequency components loss. This is because that higher frequencies have smaller effective depths and are affected by surface rust more than lower frequencies. As a result, non-zero centroid frequency reduction Δf_c occurs to corroded steel rod models; (4) when measuring TOF from dispersive ultrasonic waves, single frequency is used on the STFT spectrogram (e.g., 1 MHz in this paper); (5) ultrasonic wave propagation velocity on different curved paths can be estimated by an empirical model described in Eq. (4); (6) six empirical equations are proposed for detecting (Eq. (1)), locating (Eq. (21)) and quantifying (Eqs. (23), (24), (25) and (26)) surface rust on a steel rod model. Based on aforementioned findings, a surface rust detection algorithm is proposed, as summarized in Fig. 14.

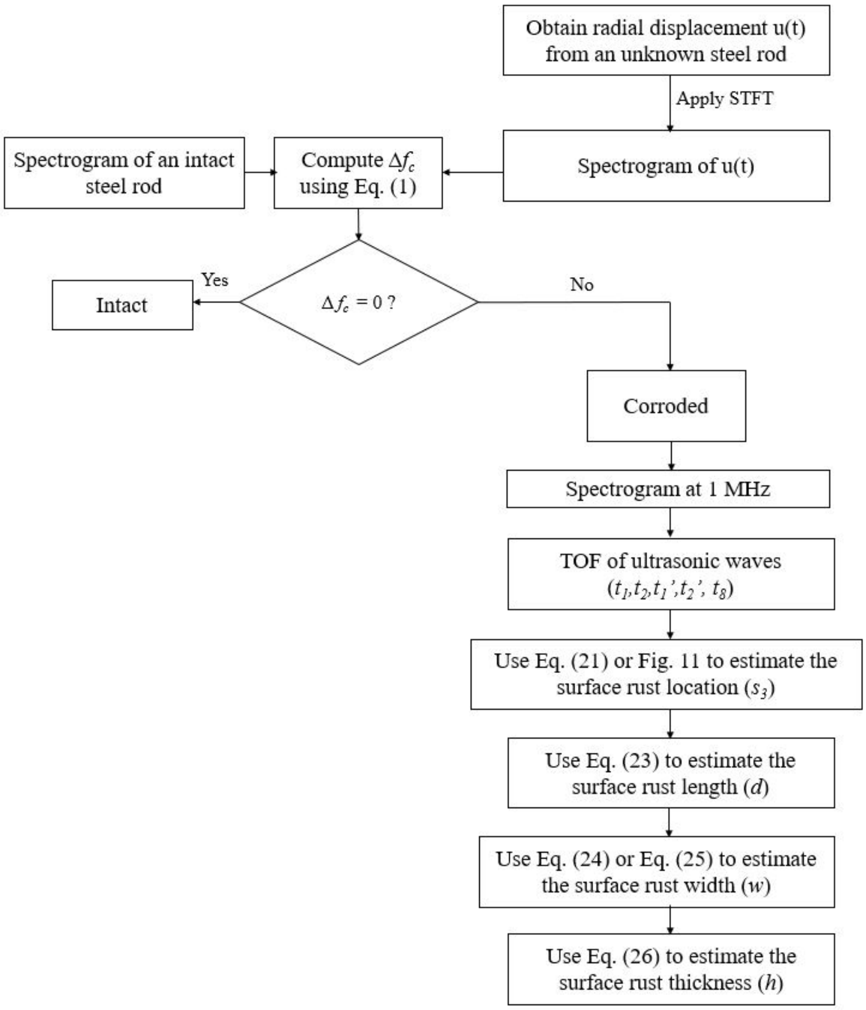

Figure 14. Surface rust detection algorithm

5. Conclusion

This paper reports a finite element study of utilizing point-source generated ultrasonic waves for detecting surface rust in steel rod models. Methods of detecting, locating and quantifying the surface rust are achieved by using the STFT (short time Fourier transform) spectrogram of radial displacement collected on the surface of corroded steel rod models. We have concluded the following.

- Presence of surface rust can be detected by the reduction of centroid frequency of the first wave packet in the STFT spectrogram of corroded steel rod models.
- Location of surface rust is estimated by finding the difference in arrival time (TOF) between helically propagating ultrasonic waves and scattered ultrasonic waves (due to surface rust).
- Length of surface rust can be predicted by calculating the difference in TOF between longitudinally propagating ultrasonic waves of intact and corroded steel rod models. This difference in TOF is related to the longitudinal dimension (length) of surface rust.
- Width of surface rust can be determined by calculating the difference in TOF of the first wave packet between intact and corroded steel rods in the STFT spectrogram at a fixed frequency (e.g., 1 MHz in this paper).
- Thickness of surface rust can be estimated by utilizing the second-order derivative of the first wave packet of corroded steel rod models.

In conclusion, this paper presents our finite element analysis of ultrasonic waves on intact and corroded steel rod models for detecting, locating, and quantifying surface rust in a systematically approach. While research result is obtained in several empirical equations, it is believed that our proposed damage detection algorithm can be applied to other corrosion detection problems using distributed photoacoustic fiber optic sensors on steel rods or steel rebars.

Acknowledgments: The authors would like to thank the National Science Foundation (NSF), Division of Civil, Mechanical and Manufacturing Innovation (CMMI) for partially supporting this research through Grant CMMI-1401369.

Author Contributions: Qixiang Tang and Tzuyang Yu conceived and designed the simulation; Qixiang Tang, Jie Hu and Cong Du analyzed the data; Xingwei Wang and Tzuyang Yu contributed analysis tools; Qixiang Tang drafted the manuscript.

Conflicts of Interest: The authors declare no conflict of interest.

1. Huston, D. *Structural Sensing, Health Monitoring, and Performance Evaluation*; 2010.
2. for Testing, A.S.; Materials. Metals Test Methods and Analytical Procedures. *1999 Annual Book of ASTM Standards* **1999**, *3*.
3. Qixiang Tang, Tzuyang Yu, M.J. Finite element analysis for the damage detection of light pole structures. *Proc.SPIE* **2015**, *9437*, 9437 – 9437 – 15.
4. Cheng, W. Pulsed Eddy Current Testing of Carbon Steel Pipes' Wall-thinning Through Insulation and Cladding. *Journal of Nondestructive Evaluation* **2012**, *31*, 215–224.
5. Wallbrink, C.; Wade, S.A.; Jones, R. The effect of size on the quantitative estimation of defect depth in steel structures using lock-in thermography. *Journal of Applied Physics* **2007**, *101*, 104907.
6. Cook, D.; Berthelot, Y. Detection of small surface-breaking fatigue cracks in steel using scattering of Rayleigh waves. *NDT & E International* **2001**, *34*, 483–492.
7. Resch, M.T.; Nelson, D.V. An ultrasonic method for measurement of size and opening behavior of small fatigue cracks. *Small-crack test methods. ASTM International*, **1992**, pp. 169–196.
8. Rodríguez, G.; Casas, J.; Villalba, S. SHM by DOFS in civil engineering: a review. "Structural Monitoring and Maintenance. *Structural monitoring and maintenance* **2015**, *2*.
9. Li, H.N.; Li, D.S.; Song, G.B. Recent applications of fiber optic sensors to health monitoring in civil engineering. *Engineering Structures* **2004**, *26*, 1647 – 1657.
10. Du, C.; OwusuTwumasi, J.; Tang, Q.; Guo, X.; Zhou, J.; Yu, T.; Wang, X. All-Optical Photoacoustic Sensors for Steel Rebar Corrosion Monitoring. *Sensors* **2018**.
11. Zou, X.; Chao, A.; Tian, Y.; Wu, N.; .; Yu, T.; Wang, X. A novel Fabry-Perot fiber optic temperature sensor for early age hydration heat study in Portland cement concrete. *Smart Structures and System* **2013**, *12*.
12. Wu, N.; Zou, X.; Zhou, J.; Wang, X. Fiber optic ultrasound transmitters and their applications. *Measurement* **2016**, *79*, 164–171.
13. Tang, Q.; Yu, T. Finite element simulation for damage detection of surface rust in steel rebars using elastic waves. *Proceedings of SPIE Vol. 9804* **2016**.
14. Sansalone, M.; Carino, N.J. Detecting Delaminations in Reinforced Concrete Slabs with and without Asphalt Concrete Overlays Using the Impact-Echo Method. *National Bureau of Standards Journal of Research* **1987**, *Nov./Dec.*, 369–381.
15. Tang, Q.; Yu, T. Finite element simulation of ultrasonic waves in corroded reinforced concrete for early-stage corrosion detection. *Proc.SPIE* **2017**, *10169*, 10169 – 10169 – 9.
16. Zhang, S.; Shen, W.; Li, D.; X.Zhang.; Chen, B. NONDESTRUCTIVE ULTRASONIC TESTING IN ROD STRUCTURE WITH A NOVEL NUMERICAL LAPLACE BASED WAVELET FINITE ELEMENT METHOD. *Latin American Journal of Solids and Structures* **2018**.
17. Tang, Q.; Twumasi, J.O.; Hu, J.; Wang, X.; Yu, T. Finite element simulation of photoacoustic fiber optic sensors for surface corrosion detection on a steel rod. *Proc.SPIE* **2018**, *10599*, 10599 – 10599 – 13.
18. Dassault Systémes, 10 rue Marcel Dassault, CS 40501, 78946 Vélizy-Villacoublay Cedex-France. *Abaqus/CAE User's Manual Version 6.12*, 2011.

Peer-reviewed version available at *Infrastructures* **2018**, *3*, 29; doi:10.3390/infrastructures3030029

19. Liu, G.R.; Quek, S.S. A non-reflecting boundary for analyzing wave propagation using the finite element method. *Fn. Elem. in Anal. Des.* **2003**, *39*, 403–417.
20. Bergmann, L. Ultrasonics and their Scientific and Technical Applications. *Wiley, New York* **1948**.
21. Viktorov, I. Rayleigh Waves and Lamb waves-Physical Theory and Application. *New York: Plenum* **1967**.